Structure of the human 26S proteasome at a resolution of 3.9 Å

Andreas Schweitzer[a,1], Antje Aufderheide[a,1], Till Rudack[b,1], Florian Beck[a], Günter Pfeifer[a], Jürgen M. Plitzko[a], Eri Sakata[a], Klaus Schulten[c,d], Friedrich Förster[a,e,2], and Wolfgang Baumeister[a,2]

[a]Department of Molecular Structural Biology, Max-Planck Institute of Biochemistry, D-82152 Martinsried, Germany; [b]Beckman Institute, University of Illinois, Urbana–Champaign, Urbana, IL 61801; [c]Beckman Institute, Department of Physics, Energy Biosciences Institute, Center for the Physics of Living Cells, University of Illinois, Urbana–Champaign, Urbana, IL 61801; [d]Center for Biophysics and Quantitative Biology, University of Illinois, Urbana–Champaign, Urbana, IL 61801; and [e]Cryo-electron Microscopy, Bijvoet Center for Biomolecular Research, Utrecht University, 3584 CH Utrecht, The Netherlands

Contributed by Wolfgang Baumeister, May 24, 2016 (sent for review May 18, 2016; reviewed by Robert M. Glaeser and Alexander Varshavsky)

Protein degradation in eukaryotic cells is performed by the Ubiquitin-Proteasome System (UPS). The 26S proteasome holocomplex consists of a core particle (CP) that proteolytically degrades polyubiquitylated proteins, and a regulatory particle (RP) containing the AAA-ATPase module. This module controls access to the proteolytic chamber inside the CP and is surrounded by non-ATPase subunits (Rpns) that recognize substrates and deubiquitylate them before unfolding and degradation. The architecture of the 26S holocomplex is highly conserved between yeast and humans. The structure of the human 26S holocomplex described here reveals previously unidentified features of the AAA-ATPase heterohexamer. One subunit, Rpt6, has ADP bound, whereas the other five have ATP in their binding pockets. Rpt6 is structurally distinct from the other five Rpt subunits, most notably in its pore loop region. For Rpns, the map reveals two main, previously undetected, features: the C terminus of Rpn3 protrudes into the mouth of the ATPase ring; and Rpn1 and Rpn2, the largest proteasome subunits, are linked by an extended connection. The structural features of the 26S proteasome observed in this study are likely to be important for coordinating the proteasomal subunits during substrate processing.

proteostasis | cryo-electron microscopy | AAA-ATPase | integrative modeling

The 26S proteasome is an ATP-dependent multisubunit protease degrading polyubiquitylated proteins (1, 2). It operates at the executive end of the Ubiquitin-Proteasome System (UPS) and has a key role in cellular proteostasis. The 26S proteasome selectively removes misfolded proteins or proteins no longer needed and it is critically involved in numerous cellular processes such as protein quality control, regulation of metabolism, cell cycle control, or antigen presentation. Malfunctions of the UPS are associated with various pathologies, including neurodegenerative diseases and cancer. Therefore, the proteasome is an important pharmaceutical target, and a high-resolution structure is a prerequisite for structure-based drug design (3).

The 26S proteasome comprises the 20S cylindrical core particle (CP), where proteolysis takes place, and 19S regulatory particles (RPs). In cellular environments, 26S holocomplexes with either one or two RPs bound to the ends of the cylinder-shaped CP coexist (4). The role of the RPs is to recruit ubiquitylated substrates, to cleave off their polyubiquitin tags, and to unfold and translocate them into the CP for degradation into short peptides. Whereas X-ray crystallography has revealed the atomic structures first of archaeal 20S proteasome (5) and subsequently of the yeast (6) and mammalian proteasome (7), only lower-resolution structures were available for the 26S holocomplex. Given the compositional and conformational heterogeneity of the RP, single-particle cryo-electron microscopy (cryo-EM) has been the most successful approach to determining the structure of the 26S holocomplex (8). At this point, the most detailed insights have been obtained for the yeast 26S proteasome (9–13), allowing model building to be accurate on the secondary structure level. Single-particle cryo-EM studies of the isolated RP lid subcomplex surpassed 4 Å resolution in some structurally invariable segments, allowing for more accurate model building for the corresponding areas (14). However, the structure of the 26S holocomplex has not been resolved at the same level of detail.

The consensus of the cryo-EM studies of the yeast 26S proteasome is that the motor core of the RP is a ring-shaped heterohexameric AAA+ (ATPase Associated with diverse Activities) ATPase, which binds to the CP. Depending on their nucleotide-bound states, the six different RP Triple-A ATPase (Rpt) subunits 1–6 adopt different conformations, which induce changes in the organization of the surrounding RP Non-ATPases (Rpns) (11, 15, 16). At least three distinct conformational states, s1–s3, underlie the three key steps of the functional cycle: substrate recruitment, irreversible commitment, and enzymatic processing. These different functions have been inferred from the different placements of ubiquitin receptors [Rpn1 (17), Rpn10 (18), and Rpn13 (19)] and the activation of the deubiquitylating enzyme (DUB) Rpn11 (20, 21), which is positioned near the mouth of the ATPase module. Two of the conformations observed in vitro, the recruitment and processing states s1 and s3, respectively, could also be observed in situ, albeit at lower resolutions by cryo-electron tomography studies (4).

Significance

The 26S proteasome is a giant protease assembled from at least 32 different canonical subunits. In eukaryotic cells it is responsible for the regulated degradation of proteins marked for destruction by polyubiquitin tags. Mainly because of the conformational heterogeneity of the 26S holocomplex, its structure determination has been challenging. Using cryo-electron microscopy single-particle analysis we were able to obtain a high-resolution structure of the human 26S proteasome allowing us to put forward an essentially complete atomic model. This model provides insights into the proteasome's mechanism of operation and could serve as a basis for structure-based drug discovery.

Author contributions: E.S., K.S., F.F., and W.B. designed research; A.S., G.P., and J.M.P. performed research; A.S., A.A., T.R., and F.B. analyzed data; and F.F. and W.B. wrote the paper.

Reviewers: R.M.G., Lawrence Berkeley National Laboratory; A.V., California Institute of Technology.

The authors declare no conflict of interest.

Freely available online through the PNAS open access option.

Data deposition: The single particle reconstruction and the atomic coordinates have been deposited in the Electron Microscopy Data Bank, www.ebi.ac.uk/pdbe/emdb/ (accession no. EMD-4002) and the Protein Data Bank, www.rcsb.org (PDB ID codes 5L4G and 5L4K), respectively.

[1]A.S., A.A., and T.R. contributed equally to this work.

[2]To whom correspondence may be addressed. Email: f.g.forster@uu.nl or baumeist@biochem.mpg.de.

This article contains supporting information online at www.pnas.org/lookup/suppl/doi:10.1073/pnas.1608050113/-/DCSupplemental.

Hitherto, only a medium-resolution structure of the human 26S proteasome was available, which suggested differences in the placement of some subunits in mammals compared with yeast (22). Here, we report an atomic model of the complete human 26S proteasome in the substrate-recruiting state s1 based on a 3.9-Å resolution cryo-EM map. The availability of an atomic structure now allows to scrutinize potential differences between yeast and human proteasomes and provides insights into nucleotide binding.

Results and Discussion

Isolation of Human 26S Proteasomes. Human 26S proteasomes were purified from erythrocytes essentially as previously described (23). The stoichiometry of proteasome subunits in the sample was analyzed by mass spectrometry in conjunction with intensity-based absolute quantification (iBAQ) (24). All canonical subunits of the CP (α_1–α_7, β_1–β_7) and the RP (Rpt1–6, Rpn1–3, Rpn5–12) are present in approximately equimolar amounts, with the exception of Rpn13. Rpn13, which is present in stoichiometric amounts in yeast, has also been found in previous studies to be essentially absent in isolated human 26S proteasomes (25). It is likely that substoichiometrically bound Rpn13 dissociates from the 26S proteasome during the isolation process because cryo-electron tomography studies of 26S proteasomes in rat neurons also indicated a substoichiometric occupancy for this proteasome component (4).

Human 26S Proteasome EM Map at 3.9-Å Resolution. The isolated human 26S proteasomes in an ATP-containing buffer were vitrified and imaged using a FEI Krios transmission electron microscope (TEM) equipped with a Falcon III direct electron detector. In the resulting micrographs (Fig. S1) the more abundant double capped (dc) 26S and the less abundant single capped (sc) 26S particles were automatically detected and subjected to single-particle analysis. Previous structural analysis of yeast dc26S particles indicated that their two RPs can adopt different uncorrelated conformational states (11, 13, 15). To "purify" a specific conformation in silico, the dc26S particles were separated into two pseudoparticles that were processed independently (*Material and Methods*). The overall reconstructions of both dc26S and sc26S particles showed a s1-like conformation of the RPs (Fig. S2), indicating that the majority of RPs adopt this conformation. Therefore, particles in other states were discarded after 3D classification, which was performed focused on one RP.

In a final step the 393,936 pseudosc26S particles and the 67,466 sc26S particles were merged and locally refined around the input angles provided as prior values with a soft-edged mask on one RP and the CP, yielding a refined reconstruction with an average resolution of 3.9 Å (Fig. 1 and Fig. S3). Local resolution determination indicated that the resolution is significantly better in the CP, the AAA-ATPase, and the helical bundle of the lid (Figs. S4 and S5).

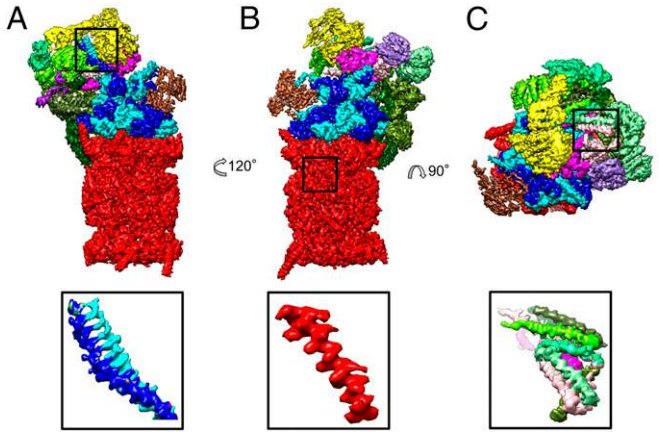

Fig. 1. Cryo-EM reconstruction of the human 26S proteasome at 3.9 Å resolution. (*A*–*C*) Three different views of the 26S proteasome colored according to its subunits. Red: CP; blue: AAA-ATPase heterohexamer; brown: Rpn1; yellow: Rpn2; green: PCI subunits (Rpn3, -5, -6, -7, -9, -12); magenta: Rpn8, -11; purple: Rpn10. (*Bottom*) Selected, magnified features (coiled-coil Rpt3/6, helix formed by residues 57–80 of β_1, a helical bundle from the lid subcomplex) from the marked areas.

Evolutionary Conservation of 26S Proteasome from Yeast to Humans. To interpret the EM map of the human 26S proteasome in the s1 state, we first fitted the s1 atomic model of the yeast 26S proteasome (11) into the human 26S map (Fig. S2). The excellent fit of the overall subunit structures and even their secondary structures indicates that the structure of the 26S proteasome is highly conserved from yeast to humans, which is consistent with the high sequence conservation of RP subunits (>30% almost throughout). The conserved 26S proteasome architecture does not confirm differences between the human 26S proteasome and the yeast structures as suggested previously (22). In particular, the locations of Rpn12 and Rpn8, which were postulated to locate to different positions, clearly remain largely invariant. The different RP architecture in ref. 22 is likely an artifact of an overestimation of the resolution, which resulted in misinterpretation of the map, as previously suggested (26).

Atomic Structure. To build an accurate atomic model of the human 26S proteasome, we followed the strategy established for large macromolecular complexes (27, 28). We first built comparative models of the human 26S proteasome subunits, extended template-free segments by de novo modeling, and superposed these human subunit models onto their respective yeast homologs. Although this initial model for the RP is largely accurate on the secondary structure level, it shows significant inaccuracies beyond, such as register shifts in helices and mispositioned loops, as it was derived from medium resolution cryo-EM data (7.7 Å) (11). Thus, differences of the atomic models of the yeast and the human 26S proteasome may reflect both interspecies variation and modeling errors. However, throughout the entire map the secondary structure elements like α-helices could be detected for all RP subunits, although with different accuracy depending on the resolution. In particular within the higher resolved regions (<4 Å) of the map such as the CP, the AAA-ATPase, and the helical bundle, the starts and ends of secondary structure elements could be clearly positioned due to the unambiguous fitting of side chains.

CP and CP-AAA Interface. The refined structure of the CP displays only minor differences compared with the bovine CP crystal structure (7). Although this conservation is inconsistent with previous low-resolution negative-stain EM analysis of the human proteasome (29), it agrees with the intermediate-resolution cryo-EM studies of the yeast 26S proteasome (9–13). Most notably, the "gate" at the entrance of the CP formed by the N termini of the α-subunits is closed as observed also in the crystal structure.

Three of the six AAA-ATPases (Rpt2, Rpt3, and Rpt5) share a C-terminal motif, a hydrophobic residue (Hb), and a tyrosine followed by a residue of any type (HbYX), which can bind to pockets in the CP (30). In the EM map, the C termini of Rpt3 and Rpt5 are clearly resolved, making it possible to discern bulky side chains (Fig. 2). In contrast, the C terminus of Rpt2 is not visible, indicating structural flexibility. Also for the yeast 26S proteasome, flexibility of one Rpt C terminus has been observed, but it has been the Rpt5 HbYX motif (13, 31). At this point we can only hypothesize why only two of three HbYX motifs bind to CP pockets in the s1 conformation of the 26S proteasome. An unbound third C terminus may facilitate rotary and lateral

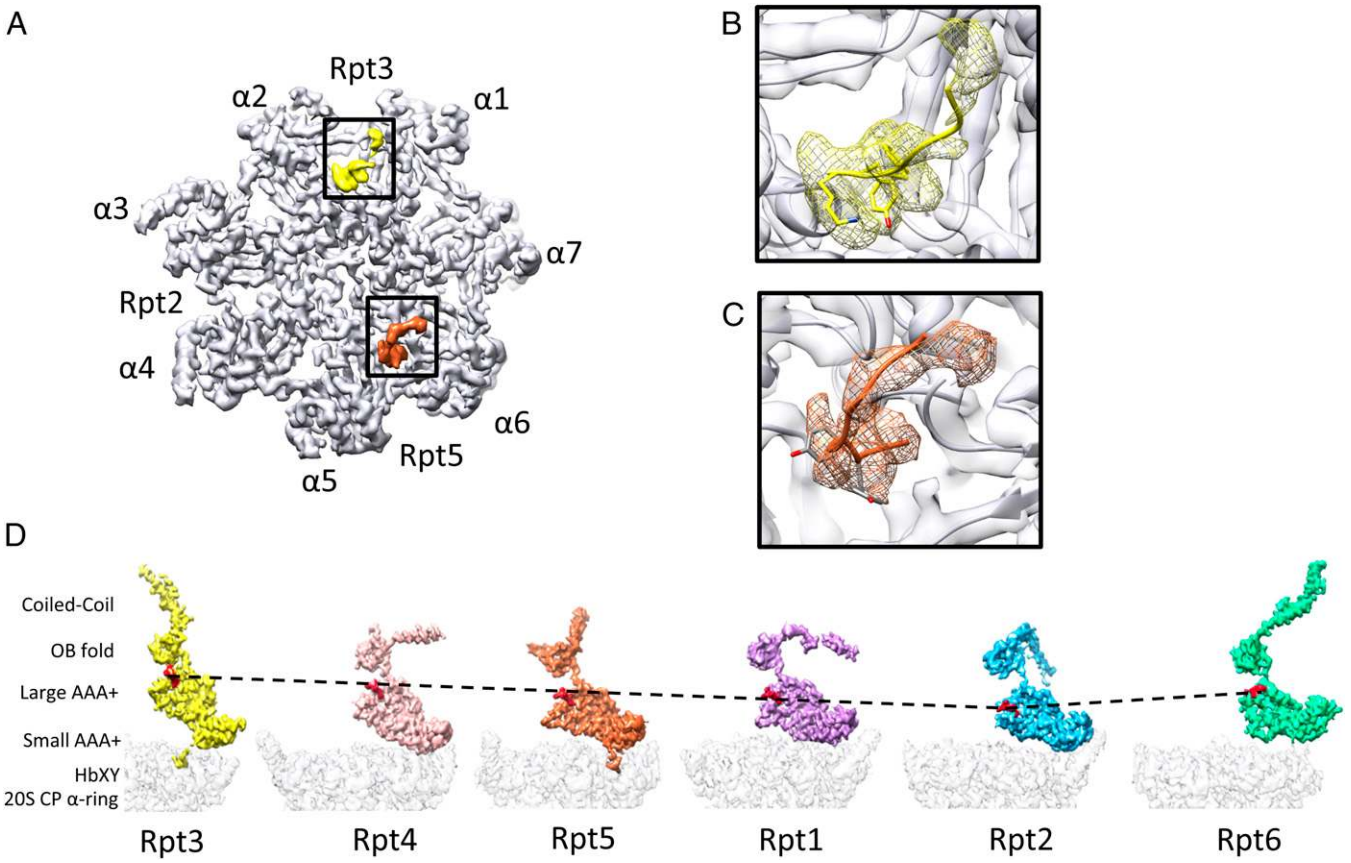

Fig. 2. Organization of AAA module. (*A*) Segmented HbXY motifs of Rpt3 (yellow) and Rpt5 (organge) located in their binding pockets of the α-ring. (*B*) Cryo-EM–based atomic model of the Rpt3 HbXY motif in the pocket formed by α_1 and α_7. (*C*) Atomic model of the Rpt5 HbXY motif in the pocket formed by α_5 and α_6. (*D*) Segmented densities of the Rpt subunits successively rotated in 60° steps around the CP axis. The different structural domains are indicated on the left. The Ar-Φ pore loops are rendered in red.

motion of the AAA module on the α-ring during the conformational changes of the 26S proteasome (11).

Organization of Rpts in Heterohexamer. In the yeast 26S proteasome the Rpt subunits assemble as an asymmetrical "split washer" in the hexamer (10). A consequence of this organization is that the aromatic hydrophobic (Ar-Φ) "pore loops," which project into the central pore of the heterohexamer, arrange in a spiral staircase. These pore loops are thought to pull the substrate into the CP (32).

Although in previous intermediate-resolution studies of the yeast 26S proteasome the precise position of the Ar-Φ pore loops has been inferred from the fitted structures of Rpt homologs, the high-resolution map of the human 26S proteasome now reveals the proteasomal Ar-Φ pore loops directly (Fig. 2*D*). Five of the six Ar-Φ pore loops position remarkably accuractely on a spiral staircase (Rpt3, -4, -5, -1, and -2, ordered by decreasing elevation), whereas the corresponding segment of Rpt6 is positioned in between.

Nucleotide Loading of AAA-ATPase Module. AAA-ATPases bind nucleotides through a site formed by the Walker A and Walker B motifs located in the large AAA subdomain (33). In many AAA-ATPases, ATP binding is further stabilized by an arginine (Arg) finger located in the AAA chain that is positioned adjacent in the hexameric ring. In the case of the Rpts, as with essentially all proteins of the classical AAA clade of the AAA+ protein family, this motif even contains two arginine residues. A consequence of the split washer organization is that only five of the six Arg–finger motifs can be engaged; the Arg–finger of Rpt3 cannot point into the binding site of Rpt6 (16).

Inspection of the cryo-EM density at the nucleotide-binding sites clearly shows nucleotide binding to each Rpt subunit, which is also apparent in the difference map of the map and the modeled protein (Fig. 3 and Fig. S6). The nucleotide density bound to Rpt6 is the smallest and can be assigned unambiguously to ADP (Fig. 3*C*). For Rpt6, the Arg–finger is not engaged in the s1 state (16), which is compatible with ADP binding (Fig. 3 *A* and *B*). The other five nucleotides are notably larger than that bound to Rpt6, and the binding of the two Arg–fingers can be clearly observed. We tentatively assigned those to ATP, but it could also be the ADP-Pi intermediate-state or an overlay of ADP- and ATP-bound structures. Higher-resolution reconstructions will be required to make this assignment unambiguous.

Full occupancy of nucleotides has previously been observed in crystal structures of some prokaryotic homologs of the Rpts. However, these fully loaded states have been considered unphysiological, and mechanistic models for ATPase function rather assume a maximum occupancy of four nucleotides in solution (34, 35). Thus, the nucleotide occupancy found in our study for the 26S proteasome in the presence of an excess of ATP indicates either that these models must be revisited or that the mechanism of the 26S proteasome deviates from its simpler prokaryotic counterparts.

Structural Features of Rpts. The high resolution throughout the entire AAA module allows the building of a complete atomic model with high confidence (Fig. 3). Interestingly, none of the Rpts shares the β-strand positioned at the N terminus of the crystal structure of the AAA domain of the archaeal Rpt homolog PAN (36). In the Rpts, the corresponding segment forms a short helix or

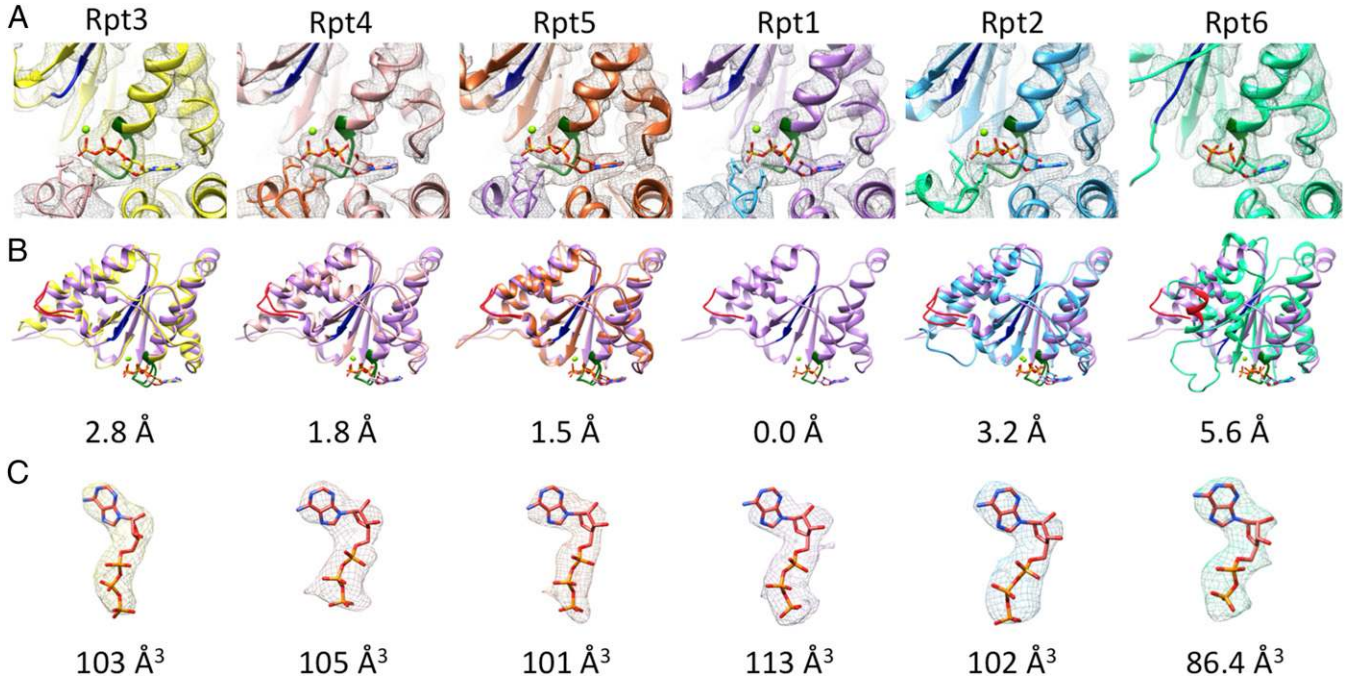

Fig. 3. Nucleotide binding and structures of large AAA subdomains. (*A*) Nucleotide densities and coordinated Mg^{2+} and Arg–fingers of the neighboring subunits at the Walker A motifs (green) of the Rpts. (*B*) Structural comparison of the large AAA+ domain of each Rpt with Rpt1 (Walker A green, Walker B dark blue, pore loop red). Below each panel the root mean squared deviation of the respective structure compared with Rpt1 in angstroms is assigned. (*C*) EM densities of bound nucleotides and modeled nucleotides. Below each panel the volume of the difference map in $Å^3$ (cubic Angstroms) is shown.

a loop (Rpt3). It is possible that the strand formation and its integration into the adjacent β-sheet in PAN is due to truncation in the crystal structure of the large AAA subdomain of PAN (36).

Comparison of the large Rpt AAA subdomains reveals that the structures of Rpt1–5 are relatively similar, but Rpt6 deviates notably (Fig. 3*B*). The most striking difference is that the Ar-Φ pore loop of Rpt6 orients differently and adopts a partially helical fold. This helix has pronounced hydrophobic contacts to the small helix at the N terminus at the large AAA subdomain (Leu219-Val140, Val220-Leu137, Phe223-Pro133). The Rpt6 pore loop does not protrude into the pore, which is consistent with Rpt6 not being part of the spiral staircase formed by the other five Ar-Φ pore loops. Further high-resolution studies of the substrate processing state of the AAA module will be required to address to what extent the unique structure of Rpt6 is mostly due to its sequence or its nucleotide-bound state.

Organization of the RP Base Subcomplex. In addition to the six Rpts of the RP, the high-resolution map also allowed modeling the Rpns almost completely (Fig. 4). The resulting structure is highly similar to that observed in the yeast 26S proteasome (8). The RP consists of two independently assembling subcomplexes, the base and the lid (37). The base consists of the Rpts and two non-ATPases: the two largest, structurally related RP subunits Rpn1 and Rpn2. Rpn1 serves as a ubiquitin receptor (17), whereas Rpn2 seems to function solely as a lid-binding scaffold. Rpn1 associates with Rpt1/2 and is the structurally most variable subunit of the RP (Fig. S4). In all intermediate-resolution reconstructions of the yeast 26S proteasome, Rpn1 was completely separate from the other Rpns. Low-pass filtering of our high-resolution map reveals a newly observed connection between Rpn1 and Rpn2 (Fig. 4*F*). This connection is likely achieved through a helix in Rpn2 ranging approximately from Glu826 to Glu852, which is located at the interface of the N-terminal helix of Rpt2 (Gln57 to Pro87) and Rpn1. The described insertion of Rpn2 connecting Rpn2 with Rpn1 and Rpt2 may facilitate coordination of rotational motions of Rpn1 and all other Rpns during transition from the s1 state to the s2 and s3 conformations (11).

Structure of the Lid Subcomplex. The lid consists of a heterohexameric horseshoe of the structurally similar Proteasome-Cyclosome-Initiation factor (PCI) subunits Rpn9, -5, -6, -7, -3, and -12. The small lid subunit Rpn15/Dss1, which was recently suggested to function as a ubiquitin receptor (38), is positioned between Rpn7 and Rpn3 (Fig. 4*E*) (14, 39). The lid shields the Rpn8/11 heterodimer, which projects the active site of Rpn11 near the mouth of the AAA module.

As previously observed for the isolated yeast lid (14), the best-resolved (better than 4 Å) and hence least flexible part of the lid is the helical bundle formed by the C-terminal segments of the lid subunits (Fig. 1 and Figs. S4 and S5). The C terminus of Rpn3, however, could not be resolved in the isolated lid. In the human 26S holocomplex we could trace it parallel to the Rpt3/6 coiled coil into the mouth of the oligosaccharide binding (OB) fold ring of the AAA module (Fig. 4*D*). We have previously proposed that this cavity forms a composite active site where substrate deubiquitylation and unfolding occurs (40). The Rpn3 C terminus may be a sensor for substrates engaged in the OB mouth that initiates conformational changes of the lid for activation of Rpn11 and hence the composite active site (15, 16). Consistent with this hypothesis, Rpn3 is located in proximal distance to the region in Rpn11 (Ile163 to His199), which we previously suggested to function as a trigger for substrate recognition (40). This region is not resolved in X-ray structures of the isolated Rpn8/Rpn11 dimer (40, 41), indicating that it is flexible in this context. In the 26S holocomplex this region is resolved and hence stabilized by Rpn2 and Rpn3.

Conclusions. The high-resolution structure of the human proteasome determined in this study reveals many details that are essential for its cellular function. This structure may serve as a starting point for future structure-guided drug discovery. AAA-ATPases have recently emerged as enzymes that can be

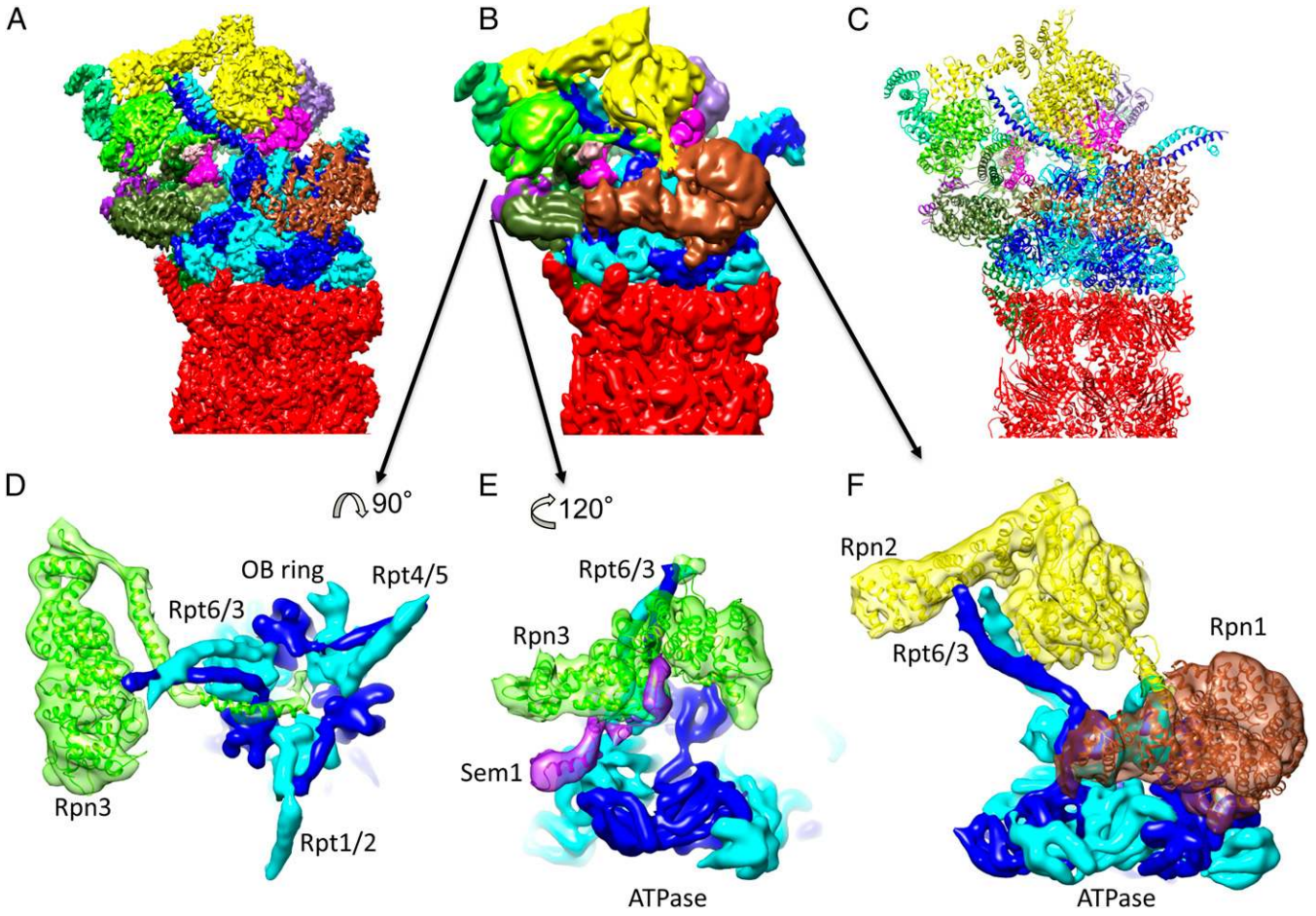

Fig. 4. Organization of Rpns and previously unresolved features. (*A*) Reconstruction filtered to 4 Å resolution and colored according to subunits. (*B*) Reconstruction filtered to 7 Å resolution and colored according to subunits. (*C*) Atomic model colored according to subunits. (*D*) Obstruction of OB ring by C terminus of Rpn3. (*E*) Interaction of Sem1 and Rpn3. (*F*) Connecting density between Rpn1 and Rpn2.

allosterically inhibited (42). For example, Rpt6, by virtue of its unique structure and distinguished role in the AAA-hetero-hexamer, is a possible target for a specific pharmacological agent.

Materials and Methods

26S Proteasome Purification and Characterization. Human 26S proteasomes were prepared from fresh human blood (23) and characterized using mass spectrometry (*SI Materials and Methods*). Samples of ∼0.5 mg/mL were quickly frozen for storage at −80 °C until use.

Data Acquisition. The dataset was collected on a Titan Krios with a Falcon III camera in movie mode using the FEI EPU software at a pixel size of 1.35 Å at the specimen level (*SI Materials and Methods*).

Image Processing. Both sc26S and dc26S particles were used to obtain the final 3.9-Å resolution reconstruction (*SI Materials and Methods* and Fig. S7). Essentially all image processing steps were carried out in TOM (43) and RELION (44).

Model Building. Initial models were obtained by comparative and de novo modeling (*SI Materials and Methods*). The human 26S proteasome subunits were positioned into the EM map according to their positions of the yeast homologs [PDB ID code 4cr2 (11)] and subsequently refined, first in real space using molecular dynamics flexible fitting (MDFF) (45) and then in reciprocal space. MDFF simulations were prepared using QwikMD (46), analyzed with VMD (47), and carried out with NAMD (48).

ACKNOWLEDGMENTS. We thank Christopher Aylett for providing a script for conversion of EM density and Fourier shell correlation into MTZ files; Andreas Bracher for assistance with reciprocal space refinement; and Maximilian Scheurer for assistance with automating the real space refinement tools. The authors acknowledge the computer time provided by the National Science Foundation (NSF)-funded Extreme Science and Engineering Discovery Environment MCA93S028 and a Blue Waters Illinois allocation, which is part of the Blue Waters sustained-petascale computing project supported by the NSF (Awards OCI-0725070 and ACI-1238993) and the state of Illinois. This work was supported by the German Science Foundation (Excellence Cluster CIPSM and SFB-1035/Project A01); NSF Grant PHY1430124; and National Institutes of Health Grant 9P41GM104601. E.S. is supported by Marie Curie Career Integration Grant. T.R. acknowledges support as a Feodor Lynen von Humboldt Postdoctoral Fellow.

1. Voges D, Zwickl P, Baumeister W (1999) The 26S proteasome: A molecular machine designed for controlled proteolysis. *Annu Rev Biochem* 68:1015–1068.
2. Finley D, Chen X, Walters KJ (2016) Gates, channels, and switches: Elements of the proteasome machine. *Trends Biochem Sci* 41(1):77–93.
3. Śledź P, Baumeister W (2016) Structure-driven developments of 26S proteasome inhibitors. *Annu Rev Pharmacol Toxicol* 56:191–209.
4. Asano S, et al. (2015) Proteasomes: A molecular census of 26S proteasomes in intact neurons. *Science* 347(6220):439–442.
5. Löwe J, et al. (1995) Crystal structure of the 20S proteasome from the archaeon T. acidophilum at 3.4 A resolution. *Science* 268(5210):533–539.
6. Groll M, et al. (1997) Structure of 20S proteasome from yeast at 2.4 A resolution. *Nature* 386(6624):463–471.
7. Unno M, et al. (2002) The structure of the mammalian 20S proteasome at 2.75 A resolution. *Structure* 10(5):609–618.
8. Förster F, Unverdorben P, Sledź P, Baumeister W (2013) Unveiling the long-held secrets of the 26S proteasome. *Structure* 21(9):1551–1562.
9. Luan B, et al. (2016) Structure of an endogenous yeast 26S proteasome reveals two major conformational states. *Proc Natl Acad Sci USA* 113(10):2642–2647.
10. Lander GC, et al. (2012) Complete subunit architecture of the proteasome regulatory particle. *Nature* 482(7384):186–191.

11. Unverdorben P, et al. (2014) Deep classification of a large cryo-EM dataset defines the conformational landscape of the 26S proteasome. *Proc Natl Acad Sci USA* 111(15): 5544–5549.
12. Lasker K, et al. (2012) Molecular architecture of the 26S proteasome holocomplex determined by an integrative approach. *Proc Natl Acad Sci USA* 109(5):1380–1387.
13. Beck F, et al. (2012) Near-atomic resolution structural model of the yeast 26S proteasome. *Proc Natl Acad Sci USA* 109(37):14870–14875.
14. Dambacher CM, Worden EJ, Herzik MA, Martin A, Lander GC (2016) Atomic structure of the 26S proteasome lid reveals the mechanism of deubiquitinase inhibition. *eLife* 5:e13027.
15. Matyskiela ME, Lander GC, Martin A (2013) Conformational switching of the 26S proteasome enables substrate degradation. *Nat Struct Mol Biol* 20(7):781–788.
16. Śledź P, et al. (2013) Structure of the 26S proteasome with ATP-γS bound provides insights into the mechanism of nucleotide-dependent substrate translocation. *Proc Natl Acad Sci USA* 110(18):7264–7269.
17. Shi Y, et al. (2016) Rpn1 provides adjacent receptor sites for substrate binding and deubiquitination by the proteasome. *Science* 351(6275):831.
18. van Nocker S, et al. (1996) The multiubiquitin-chain-binding protein Mcb1 is a component of the 26S proteasome in Saccharomyces cerevisiae and plays a nonessential, substrate-specific role in protein turnover. *Mol Cell Biol* 16(11):6020–6028.
19. Husnjak K, et al. (2008) Proteasome subunit Rpn13 is a novel ubiquitin receptor. *Nature* 453(7194):481–488.
20. Yao T, Cohen RE (2002) A cryptic protease couples deubiquitination and degradation by the proteasome. *Nature* 419(6905):403–407.
21. Verma R, et al. (2002) Role of Rpn11 metalloprotease in deubiquitination and degradation by the 26S proteasome. *Science* 298(5593):611–615.
22. da Fonseca PC, He J, Morris EP (2012) Molecular model of the human 26S proteasome. *Mol Cell* 46(1):54–66.
23. Liu CW, et al. (2006) ATP binding and ATP hydrolysis play distinct roles in the function of 26S proteasome. *Mol Cell* 24(1):39–50.
24. Schwanhäusser B, et al. (2011) Global quantification of mammalian gene expression control. *Nature* 473(7347):337–342.
25. Chen X, Lee BH, Finley D, Walters KJ (2010) Structure of proteasome ubiquitin receptor hRpn13 and its activation by the scaffolding protein hRpn2. *Mol Cell* 38(3): 404–415.
26. Lander GC, Martin A, Nogales E (2013) The proteasome under the microscope: The regulatory particle in focus. *Curr Opin Struct Biol* 23(2):243–251.
27. Goh BC, et al. (2016) Computational methodologies for real-space structural refinement of large macromolecular complexes. *Annu Rev Biophys* 45:253–278.
28. Perilla JR, et al. (2015) Molecular dynamics simulations of large macromolecular complexes. *Curr Opin Struct Biol* 31:64–74.
29. da Fonseca PC, Morris EP (2008) Structure of the human 26S proteasome: Subunit radial displacements open the gate into the proteolytic core. *J Biol Chem* 283(34): 23305–23314.
30. Smith DM, et al. (2007) Docking of the proteasomal ATPases' carboxyl termini in the 20S proteasome's alpha ring opens the gate for substrate entry. *Mol Cell* 27(5): 731–744.
31. Tian G, et al. (2011) An asymmetric interface between the regulatory and core particles of the proteasome. *Nat Struct Mol Biol* 18(11):1259–1267.
32. Nyquist K, Martin A (2014) Marching to the beat of the ring: Polypeptide translocation by AAA+ proteases. *Trends Biochem Sci* 39(2):53–60.
33. Wendler P, Ciniawsky S, Kock M, Kube S (2012) Structure and function of the AAA+ nucleotide binding pocket. *Biochim Biophys Acta* 1823(1):2–14.
34. Sauer RT, Baker TA (2011) AAA+ proteases: ATP-fueled machines of protein destruction. *Annu Rev Biochem* 80:587–612.
35. Smith DM, Fraga H, Reis C, Kafri G, Goldberg AL (2011) ATP binds to proteasomal ATPases in pairs with distinct functional effects, implying an ordered reaction cycle. *Cell* 144(4):526–538.
36. Zhang F, et al. (2009) Structural insights into the regulatory particle of the proteasome from Methanocaldococcus jannaschii. *Mol Cell* 34(4):473–484.
37. Glickman MH, et al. (1998) A subcomplex of the proteasome regulatory particle required for ubiquitin-conjugate degradation and related to the COP9-signalosome and eIF3. *Cell* 94(5):615–623.
38. Paraskevopoulos K, et al. (2014) Dss1 is a 26S proteasome ubiquitin receptor. *Mol Cell* 56(3):453–461.
39. Bohn S, et al. (2013) Localization of the regulatory particle subunit Sem1 in the 26S proteasome. *Biochem Biophys Res Commun* 435(2):250–254.
40. Pathare GR, et al. (2014) Crystal structure of the proteasomal deubiquitylation module Rpn8-Rpn11. *Proc Natl Acad Sci USA* 111(8):2984–2989.
41. Worden EJ, Padovani C, Martin A (2014) Structure of the Rpn11-Rpn8 dimer reveals mechanisms of substrate deubiquitination during proteasomal degradation. *Nat Struct Mol Biol* 21(3):220–227.
42. Banerjee S, et al. (2016) 2.3 Å resolution cryo-EM structure of human p97 and mechanism of allosteric inhibition. *Science* 351(6275):871–875.
43. Nickell S, et al. (2005) TOM software toolbox: Acquisition and analysis for electron tomography. *J Struct Biol* 149(3):227–234.
44. Scheres SH (2012) RELION: Implementation of a Bayesian approach to cryo-EM structure determination. *J Struct Biol* 180(3):519–530.
45. Trabuco LG, Villa E, Schreiner E, Harrison CB, Schulten K (2009) Molecular dynamics flexible fitting: A practical guide to combine cryo-electron microscopy and X-ray crystallography. *Methods* 49(2):174–180.
46. Ribeiro JV, et al. (2016) QwikMD-Integrative Molecular Dynamics Toolkit for novices and experts. *Sci Rep* 6:26536–26540.
47. Humphrey W, Dalke A, Schulten K (1996) VMD: Visual molecular dynamics. *J Mol Graph* 14(1):33–38, 27–28.
48. Phillips JC, et al. (2005) Scalable molecular dynamics with NAMD. *J Comput Chem* 26(16):1781–1802.
49. Cox J, et al. (2014) Accurate proteome-wide label-free quantification by delayed normalization and maximal peptide ratio extraction, termed MaxLFQ. *Mol Cell Proteomics* 13(9):2513–2526.
50. Steen H, Mann M (2004) The ABC's (and XYZ's) of peptide sequencing. *Nat Rev Mol Cell Biol* 5(9):699–711.
51. Aufderheide A, et al. (2015) Structural characterization of the interaction of Ubp6 with the 26S proteasome. *Proc Natl Acad Sci USA* 112(28):8626–8631.
52. Li X, et al. (2013) Electron counting and beam-induced motion correction enable near-atomic-resolution single-particle cryo-EM. *Nat Methods* 10(6):584–590.
53. Rohou A, Grigorieff N (2015) CTFFIND4: Fast and accurate defocus estimation from electron micrographs. *J Struct Biol* 192(2):216–221.
54. Scheres SH (2014) Beam-induced motion correction for sub-megadalton cryo-EM particles. *eLife* 3:e03665.
55. Cardone G, Heymann JB, Steven AC (2013) One number does not fit all: Mapping local variations in resolution in cryo-EM reconstructions. *J Struct Biol* 184(2):226–236.
56. Goddard TD, Huang CC, Ferrin TE (2007) Visualizing density maps with UCSF Chimera. *J Struct Biol* 157(1):281–287.
57. Harshbarger W, Miller C, Diedrich C, Sacchettini J (2015) Crystal structure of the human 20S proteasome in complex with carfilzomib. *Structure* 23(2):418–424.
58. Sali A, Blundell TL (1993) Comparative protein modelling by satisfaction of spatial restraints. *J Mol Biol* 234(3):779–815.
59. He J, et al. (2012) The structure of the 26S proteasome subunit Rpn2 reveals its PC repeat domain as a closed toroid of two concentric α-helical rings. *Structure* 20(3): 513–521.
60. Leaver-Fay A, et al. (2011) ROSETTA3: An object-oriented software suite for the simulation and design of macromolecules. *Methods Enzymol* 487:545–574.
61. Kaufmann KW, Lemmon GH, Deluca SL, Sheehan JH, Meiler J (2010) Practically useful: What the Rosetta protein modeling suite can do for you. *Biochemistry* 49(14): 2987–2998.
62. Trabuco LG, Villa E, Mitra K, Frank J, Schulten K (2008) Flexible fitting of atomic structures into electron microscopy maps using molecular dynamics. *Structure* 16(5): 673–683.
63. Mackerell AD, Jr, Feig M, Brooks CL, III (2004) Extending the treatment of backbone energetics in protein force fields: Limitations of gas-phase quantum mechanics in reproducing protein conformational distributions in molecular dynamics simulations. *J Comput Chem* 25(11):1400–1415.
64. Stone JE, McGreevy R, Isralewitz B, Schulten K (2014) GPU-accelerated analysis and visualization of large structures solved by molecular dynamics flexible fitting. *Faraday Discuss* 169:265–283.
65. Tyka MD, et al. (2011) Alternate states of proteins revealed by detailed energy landscape mapping. *J Mol Biol* 405(2):607–618.
66. Lindert S, McCammon JA (2015) Improved cryoEM-Guided Iterative Molecular Dynamics: Rosetta protein structure refinement protocol for high precision protein structure prediction. *J Chem Theory Comput* 11(3):1337–1346.
67. Greber BJ, et al. (2014) The complete structure of the large subunit of the mammalian mitochondrial ribosome. *Nature* 515(7526):283–286.
68. Adams PD, et al. (2002) PHENIX: Building new software for automated crystallographic structure determination. *Acta Crystallogr D Biol Crystallogr* 58(Pt 11): 1948–1954.
69. Emsley P, Lohkamp B, Scott WG, Cowtan K (2010) Features and development of Coot. *Acta Crystallogr D Biol Crystallogr* 66(Pt 4):486–501.